ELSEVIER

Spectral signature of highly turbid waters
Application with SPOT data to quantify suspended particulate
matter concentrations

David Doxaran[a,*], Jean-Marie Froidefond[a], Samantha Lavender[b], Patrice Castaing[a]

[a]Département de Géologie et Océanographie, Université Bordeaux I, UMR 5805 EPOC Avenue des Facultés, 33405 Talence Cedex, France
[b]Institute of Marine Studies, University of Plymouth, Drake Circus, Plymouth, Devon PL4 8AA, UK

Abstract

An experimental method for determining water composition from "ocean colour" satellite data, in visible and near-infrared (NIR) wavelengths, is applied to highly turbid waters. Numerous spectroradiometric measurements are carried out in the Gironde estuary, for suspended particulate matter (SPM) concentrations ranging between 35 and more than 2000 mg l^{-1}. Empirical relationships are established between remote-sensing reflectance (R_{rs}) in SPOT-HRV bands and SPM concentration through these numerous in situ measurements. We observed that remote-sensing reflectance increases with SPM concentration and that the SPOT bands saturate at the highest turbidities. The best correlations are obtained for the NIR band XS3 (790–890 nm) and for the reflectance ratios: $R_{rs}(XS3)/R_{rs}(XS1)$ and $R_{rs}(XS3)/R_{rs}(XS2)$. The XS1 and XS2 visible bands are only used to determine SPM concentrations in the lower part of the estuary (where the SPM concentrations are lower). As a result, SPM concentrations within the surface waters in the estuary are estimated up to 2000 mg l^{-1} with an accuracy better than ±35%. The algorithm is finally applied to a SPOT scene. Satellite data are corrected for atmospheric effects using a radiative transfer code and in situ reflectance measurements; as a result, the horizontal distribution of SPM is retrieved. Moreover, the high spatial resolution HRV-SPOT sensor shows detailed sedimentary flows, especially in the visible XS1 and XS2 spectral bands. © 2002 Elsevier Science Inc. All rights reserved.

Keywords: Reflectance; Estuary; Gironde; SPOT; Sediment

1. Introduction

In clear oceanic Case 1 waters (Morel & Prieur, 1977), algorithms are used to interpret satellite data in terms of chlorophyll concentration (O'Reilley et al., 1998), and hence, deduce primary production (Antoine, Morel, & André, 1995; Morel, 1988). The signal becomes more complicated in coastal and estuarine Case 2 waters where terrestrial substances, such as coloured dissolved organic matter (CDOM or yellow substances) and suspended particles, are present in addition to phytoplankton. In these turbid waters, incident light scattering by suspended particulate matter (SPM), and therefore the attenuation of light

within the water column, is important (Gordon & McCluney, 1975; Ivanoff, 1975; Morel, 1991). Therefore, SPM has an inhibitive effect on primary production in coastal waters and its detection is essential in understanding biological mechanisms. The quantification of SPM is also necessary to design dredging strategies on navigational channels and to estimate the fluvial solid discharges to the ocean.

The interpretation of satellite imagery in coastal Case 2 areas often involves the calculation of empirical relationships between the parameters of interest and in situ optical measurements. In this way, numerous studies have looked at turbid plumes (e.g., Anji Reddy, 1993; Forget & Ouillon, 1998; Froidefond, Castaing, Mirmand, & Ruch, 1991; Ouillon, Forget, Froidefond, & Naudin, 1997; Siegel, Gerth, & Mutzke, 1999) and have quantified (to an appropriate precision) the fluvial suspended matter discharges to the ocean. Recent works have

---

* Corresponding author.
E-mail addresses: d.doxaran@geocean.u-bordeaux.fr (D. Doxaran), slavender@plymouth.ac.uk (S. Lavender).

attempted to derive SPM concentrations, and hence, fluxes in estuaries (Moore, Aiken, & Lavender, 1999; Robinson, Morris, & Dyer, 1998); the results are encouraging, but significant effort is required to reduce the retrieval uncertainty (about ±50%).

The Gironde estuary (southwest France) is an extreme example of Case 2 waters, as SPM concentrations in surface waters can reach more than 2 g/l. The objective is to determine SPM concentrations with high-resolution remotely sensed data, in order to quantify the sedimentary fluxes and to improve the validation of two hydrodynamic and transport numerical models recently adapted to the estuary (Sottolichio, Le Hir, & Castaing, 2001).

In situ spectroradiometric measurements, carried out since 1996, constitute an important optical database that will aid in the understanding of coastal waters. The in situ optical measurements include the remote-sensing reflectance (R_{rs}, sr^{-1}) defined as (Mobley, 1999) (Eq. (1)):

$$R_{rs} \ (sr^{-1}) = \frac{L_w}{E_d},\qquad(1)$$

where L_w ($W \ m^{-2} \ sr^{-1} \ nm^{-1}$) is the water-leaving radiance and E_d ($W \ m^{-2} \ nm^{-1}$) is the downwelling irradiance incident on the water surface. These in situ spectra were used to establish algorithms to quantify SPM concentrations in the Gironde estuary. Particular care was taken to correct for the skylight reflection, which perturbs above-water surface radiometric measurements. Algorithms were applied to a SPOT scene, according that SPOT-HRV high-spatial resolution imagery is suitable for monitoring small-scale areas. The three spectral bands are: XS1 (500–590 nm) and XS2 (610–680 nm) visible wavelengths, XS3 (790–890 nm) NIR wavelengths.

2. The study area

The Gironde estuary (Fig. 1), southwest France, gives a good example of sediment-dominated Case 2 waters influenced by river inputs. The origin of the particles is twofold: the two rivers' (Garonne and Dordogne) inputs and erosion of recently settled sediments by tidal currents (Castaing, 1981). The suspended matter is a mixture of organic and mineral composites, where the organic fraction represents only 1.8% of the total material (Jouanneau & Latouche, 1981). The mineral fraction is composed of micas (63%) and quartz (25%), while clay phases contain four minerals: montmorillonite (30%), illite and interstratified minerals (40%), kaolinite (15%), chlorite and interstratified minerals (15%). The grain-size distribution is: <2 μm: 47%; 2–15 μm: 40%; 16–63 μm: 9%; >63 μm: 4% (Jouanneau & Latouche, 1981). Recent measurements, in the Gironde mouth (Weber, Jouanneau, Ruch, & Mirmand, 1991), showed that a mean grain-size varied between 7.1 and 12.7 μm. The dimensions of the flocculated particles, 1 m below the water surface, were meas-
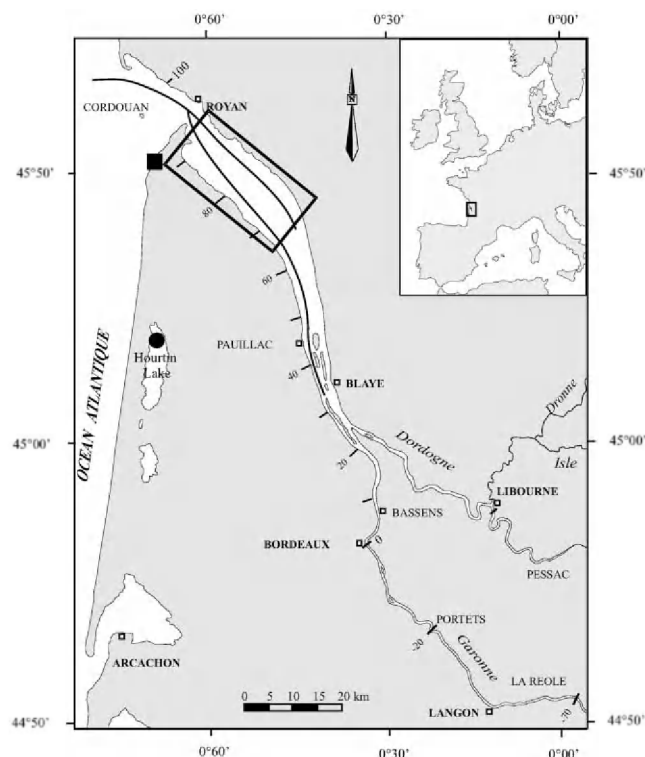

Fig. 1. The Gironde estuary, located in southwest France. The lines represent the main navigation channels; the box locates the part of the estuary analysed with the SPOT image. The black circle is the lake target and the black square represents the Soulac beaches used for the atmospheric correction.

ured by Eisma et al. (1991) with a system of video cameras. The mean diameter, practically independent of SPM concentration, was around 120 μm. Moreover, the nature and grain-size of the particles vary little with the seasons (Castaing, 1981; Eisma & Li, 1993). Chlorophyll-a (Chl-a) and CDOM concentrations are low, with Chl-a ranging from 1 to 3 μg l^{-1} (Irigoien & Castel, 1997), and dissolved organic carbon (DOC) ranging from 1 to 7 mgC l^{-1} (Abril et al., 1999).

The Gironde estuary has well-developed turbidity maximum, with both tidal asymmetry and density residual circulation involved in its formation (Castaing & Allen, 1981). The estimated total sediment mass in the turbidity maximum/fluid mud system is about 5×10^6 tons, which represents 2 years of riverine solid input (Jouanneau & Latouche, 1981). The high-turbidity zone is characterised by mean SPM concentrations of about 1 g/l (Allen, Salomon, Bassoullet, Du Penhoat, Degranpré, 1980; Allen, Sauzay, Castaing, & Jouanneau, 1977) and recent numerical simulations (Sottolichio et al., 2001) clearly demonstrated the tidal origin of the turbidity maximum. Salinity-induced density effects (Sottolichio et al., 2001) probably do not contribute to its formation, but they appear essential to retain SPM in the lower parts of the estuary and maintain the stable mass of the turbidity maximum.

3. Measurements

3.1. In situ measurements

In situ measurements were carried out in the estuary during the SEDIGIR (21st June, 29th June, and 22nd July 1996), PNOCTEL-97 (from 23rd June to 1st July 1997) oceanographic surveys. Above-water radiance measurements have been taken since 1996 in the estuary to validate ocean colour satellite data, with a co-incident water sample for each optical measurement. The optical sensor is a Spectron SE-590 spectroradiometer, with a high-resolution recorder and acceptance angle of 6° (field of view), which measures radiances between 380 and 1100 nm in 256 channels. The measurement procedure (Fig. 2) was described in detail by Whitlock et al. (1981) and is summarised as follows:

- an upwelling radiance spectrum $L_u(\lambda)$ is measured when the sensor views vertically ($\theta = 0$) the water surface (Fig. 2a); around five measurements are averaged to give the final $L_u(\lambda)$ value;
- a downwelling radiance spectrum $L_d(\lambda)$ is measured when the sensor views a Lambertian Spectralon plate (standard, Labsphere so:9917), with a reflectance factor $R_p(\lambda)$ of between 0.103 and 0.107 (Fig. 2b);
- a skylight radiance spectrum $L_s(\lambda)$ is measured when the sensor views the zenith ($\theta = 180°$) (Fig. 2c);
- a water sample is taken at a depth of between 0 and 1 m. SPM concentration is determined by filtering the water sample on Whatman GF/F glass-fibre filters (diameter: 47 mm; pore size: 0.44 μm).

The sensor was placed 3 m above the surface while measuring L_u and 20 cm above the Spectralon plate when measuring L_d.

The plate is a Lambertian target for solar zenith angles (θ_s) between 0° and 40°, as its reflectance varies by only 3% (Dilligeard, 1997). In these conditions, the downwelling
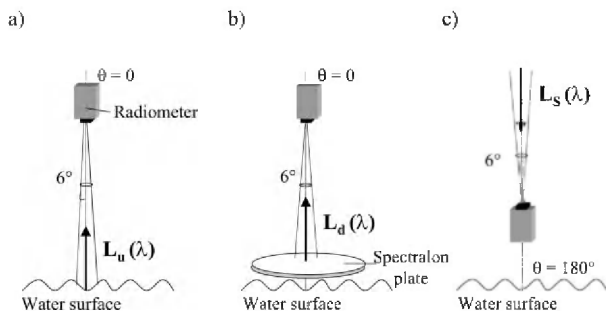

Fig. 2. In situ reflectance measurement procedure: (a) Measuring the upwelling radiance, $L_u(\lambda)$; (b) Measuring the downwelling radiance, $L_d(\lambda)$; (c) Measuring the sky radiance, $L_s(\lambda)$.

irradiance E_d (μW m^{-2} nm^{-1}) is given by the following relationship (Eq. (2)):

$$E_d(\lambda) = \pi \frac{1}{R_p(\lambda)} L_d(\lambda), \tag{2}$$

where λ (nm) is the wavelength.

The total remote-sensing reflectance T_{rs} (sr^{-1}) is then calculated as follows (Eq. (3)):

$$T_{rs}(\lambda) = R_p(\lambda) \frac{L_u(\lambda)}{\pi L_d(\lambda)} = \frac{L_u(\lambda)}{E_d(\lambda)}. \tag{3}$$

Above-water radiances $L_u(\lambda)$ were corrected for skylight reflection effects (sky glint) as a part of the incident light is directly reflected by the air–water interface (Fougnie, Frouin, Lecomte, & Deschamps, 1999; Mobley, 1999). The above-water radiance $L_u(\lambda)$ is therefore (Mobley, 1999) (Eq. (4)):

$$L_u(\lambda) = L_w(\lambda) + L_r(\lambda), \tag{4}$$

where L_w is the water-leaving radiance and L_r is the sky radiance directly reflected by the surface.

L_r can be estimated from sky radiance (L_s) measurements (Mobley, 1999):

$$L_r = \rho L_s, \tag{5}$$

where ρ is a proportional factor which relates the sky radiance (L_s) to the radiance directly reflected by the surface (L_r). The water-leaving radiance (L_w) is then (Eq. (6)):

$$L_w(\lambda) = L_u(\lambda) - \rho L_s(\lambda). \tag{6}$$

The ρ value was assumed to be wavelength-independent and the value 0.02 (Austin, 1974) was considered. In fact, the ρ factor varies with viewing geometry, sky conditions (clear, cloudy, overcast), sea surface roughness (depending on wind), and is wavelength-dependent under a cloudy sky (Fougnie et al., 1999; Mobley, 1999). Mobley used radiative transfer code to estimate cloud effects on ρ value, for uniform sky radiance distribution and for a wind speed of 10 m s^{-1}. He obtained a ρ value of 0.337 for a clear sky, a ρ value depending on wavelength for a sky with a single cumulus cloud [ρ(XS1) = 0.0392, ρ(XS2) = 0.0452, ρ(XS3) = 0.0635].

The influence of skylight reflection can be estimated from typical in situ measurements of upwelling and sky radiance (L_u and L_s in μW m^{-2} sr^{-1} nm^{-1}) (integration time of 4/64 s), carried out under a clear blue sky on 21st July 2000 at 12:35 (local time) where the SPM concentration was 158 mg l^{-1}. As the water surface was flat, the four consecutive L_u measurements are practically identical. Between 400 and 1000 nm, sky radiance is low in NIR wavelengths (700–1000 nm), moderate in red wavelengths (600–700 nm), and reaches its maximum in green–yellow wavelengths (450–550 nm). According to Eq. (5) and in situ measurements of sky radiance (Fig. 3), the skylight reflection effects were minima in the NIR band (XS3),
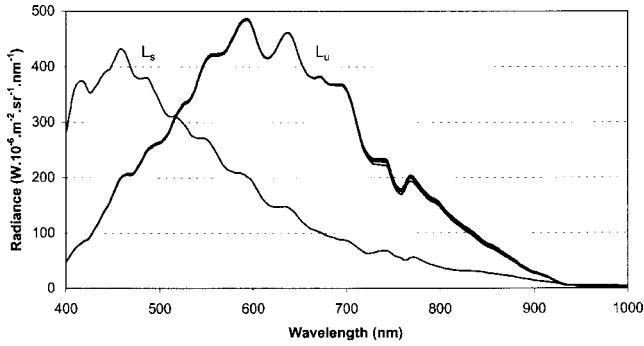
Fig. 3. Upwelling and sky radiance ($L_u(\lambda)$ and $L_s(\lambda)$ in $\mu W\ m^{-2}\ sr^{-1}$ μm^{-1}) measurements carried out at Pauillac, on 21st July 2000 at 12:35 (local time), under a clear blue sky. SPM concentration is 158 mg l^{-1}.

moderate in XS2, and at a maximum in XS1. As an example, the radiance directly reflected by the water surface ($L_r = \rho L_s$) was calculated for the ρ value of 0.02 (Austin, 1974) and for ρ values determined by Mobley (1999) for different sky conditions (clear sky, sky with single cumulus cloud, and sky with scattered cumulus clouds). The percentage of the measured upwelling radiance due to skylight reflection effects was then estimated by dividing the reflected radiance (ρL_s) by L_u. Results (Table 1) show that the $\rho L_s(\lambda)/L_u(\lambda)$ ratio is always lower than 3% in XS1, lower than 2% in XS2 and XS3. Percentage errors committed when considering a ρ value of 0.02 instead of values given by Mobley (Table 1) are lower than 1% under a clear sky and lower than 1.4% under the considered cloudy skies. For a flat sea surface and clear sky conditions, skylight reflection effects are therefore weak in visible and NIR wavelengths and sufficiently corrected when considering the 0.02 ρ value. Under these conditions, an above-water upwelling radiance measurement over highly turbid waters is a good estimation of the water-leaving radiance, i.e., the radiance due to skylight reflection (L_r) is practically insignificant compared to the water-leaving radiance (L_w).

Above-water measured upwelling spectra can be affected by Sun glint from the sea surface due to waves or foam. In most of coastal waters, light absorption by pure water is dominant in the NIR (970–1000 nm) and the water-leaving radiance L_w (970–1000 nm) is zero (Ouillon et al., 1997). Sun glint effects are then corrected by subtracting the measured L_u (970–1000 nm) to the whole L_u spectrum This assumption is not yet true in highly turbid waters because reflectance over minerals is far from zero in the NIR. Then, a particular care was taken to eliminate L_u spectra affected by Sun glint. When the water surface is plane, which is generally the case in the Gironde estuary, several successively measured L_u spectra are practically superimposed (Fig. 3) and we assume that Sun glint effects can be neglected. During a measurement, when an L_u spectrum was greater than the four other spectra, it was considered affected by Sun glint and deleted.

In order to establish SPOT empirical relationships, the $R_{rs}(\lambda)$ spectra were used to simulate SPOT (XS1, XS2, and

XS3) reflectance values. Then, the $R_{rs}(\lambda)$ values between 500–590 nm, 610–680 nm, and 790–890 nm were weighed by sensitivity to obtain $R_{rs}(XS1)$, $R_{rs}(XS2)$, and $R_{rs}(XS3)$, respectively.

3.2. Satellite data and atmospheric corrections

A SPOT scene was acquired on 14th July 1996 at 11:23 UT and covers the whole estuary. For each band, Eq. (10) was used to convert the digital numbers (DNs) into radiance units (Eq. (7)):

$$L^* = \frac{DN}{A_k},\qquad(7)$$

where L^* (W $m^{-2}\ sr^{-1}\ \mu m^{-1}$) is the top of atmosphere (TOA) upwelling radiance and A_k (W$^{-1}\ m^2$ sr μm) is the calibration factor for spectral band k, given by SPOT-Image.

L^* was converted to TOA reflectance, R^* (unitless) using the following relationship (Vermote, Tanre, Deuze, Herman, & Morcrette, 1997) (Eq. (8)):

$$\frac{R^*(XSi) = \pi L^*(XSi)}{\mu_s E_s(XSi),}\qquad(8)$$

where $i = 1$, 2, or 3 for XS1, XS2, XS3; $\mu_s = \cos(\theta_s)$, θ_s is the solar zenith angle; $E_s(XSi)$ (W $m^{-2}\ \mu m$) is the solar TOA irradiance (1865, 1615, and 1090 W $m^{-2}\ \mu m$ in channel XS1, XS2, and XS3, respectively).

The TOA measurements were then corrected for atmospheric effects using the 6s radiative transfer simulation software (Vermote et al., 1997). R^* is related to the above-water reflectance (R_w, unitless) following the relationship (Eq. (9)):

$$R^* = T_g[R_{aer} + R_{ray} + T_d R_w],\qquad(9)$$

where R_{aer} and R_{ray} (unitless) are the aerosol and Rayleigh reflectances, respectively; T_g and T_d (unitless) are the gaseous and diffuse transmittances, respectively.

Table 1
Upwelling radiance (L_u) and sky radiance (L_s) recorded at Pauillac, 21st July 2000 at 12:35 (local time), in SPOT spectral bands (XS1, XS2, and XS3)

SPOT spectral band	XS1	XS2	XS3
L_u ($\mu W\ m^{-2}\ sr^{-1}\ nm^{-1}$)	398.54	425.93	97.92
L_s ($\mu W\ m^{-2}\ sr^{-1}\ nm^{-1}$)	260.42	129.54	29.58
$(\rho L_s)/(L_u)$ (%) ($\rho = 0.02$; Austin, 1974)	1.31	0.61	0.61
(a) $(\rho L_s)/(L_u)$ (%) (clear sky)	2.20 (0.89)	1.02 (0.41)	1.02 (0.41)
(b) $(\rho L_s)/(L_u)$ (%) (single cumulus cloud)	2.56 (1.25)	1.37 (0.76)	1.92 (1.31)

The $(\rho L_s)/(L_u)$ values represent the percentage of total measured upwelling radiance (L_u) due to skylight reflection (ρL_s). Percentages are calculated for ρ values determined by Mobley (1999) for different sky conditions: (a) clear sky ($\rho = 0.0337$); sky with single cumulus cloud [$\rho(XS1) = 0.0392$, $\rho(XS2) = 0.0452$, $\rho(XS3) = 0.0635$]; Percentage errors committed when considering the Austin (1974) ρ value are noted in parentheses.

The final atmospherically corrected reflectance (R_{ac}, unitless) is:

$$R_{ac} = \frac{R_w}{1 + SR_w}, \tag{10}$$

where S (unitless) is the total spherical albedo.

This atmospherically corrected reflectance, divided by π steradians, can be compared to the remote-sensing reflectance: $1/\pi R_{ac}(\lambda) \approx R_{rs}(\lambda)$.

Atmospheric effects take into account gaseous (oxygen, ozone, water vapour, etc.) transmittance, molecular scattering and extinction (Rayleigh), aerosol scattering and extinction. The 6s model also corrects for skylight reflection (Sun glint and sky glint) following the Snell–Fresnel laws, environmental effects, and directional target effects.

In order to estimate the atmospheric composition over the study area, at the moment of the satellite's overpass, an appropriate atmospheric model was selected: the "midlatitude summer" standard model, which defines pressure (mb), temperature (K), water vapour and ozone densities (g m^{-3}) as functions of altitude (km). Of the three predefined tropospheric aerosol models (Continental, Maritime, and Urban), a model with 90% continental and 10% maritime aerosols was selected as it took into account the eastern winds blowing from the land.

The aerosol optical thickness (at 550 nm) is obtained by integrating the total extinction coefficient, K_{550} (km^{-1}) (Eq. (11)):

$$\tau(550) = \int_0^\infty K_{550}(z)dz. \tag{11}$$

The total extinction coefficient is defined as (Eq. (12)):

$$K_{550}(z) = \sigma_{550}10^{-3}N(z) \tag{12}$$

where σ_{550} (μm^2) is the extinction cross-section and the aerosol density (N, part./cm^3) is a function of visibility (v, km) (Eq. (13)):

$$N(z) = \frac{a(z)}{v} + b(z), \tag{13}$$

where z is the altitude (km). This relationship was determined by McClatchey, Fenn, Selby, Volz, and Garing (1971), with $a(z)$ and $b(z)$ expressed in part./cm^2 and part./cm^3, respectively.

In this research, the visibility measurements were obtained from the national meteorology survey (METEO-FRANCE) at Bordeaux-Mérignac airport, 20 km far from the study area.

In situ reflectance measurements were used to improve and validate the atmospheric corrections. Target areas, with known in situ reflectances, were identified on the imagery; they are Médoc beaches and Hourtin lake, located to the west of the estuary (Fig. 1). Following Chavez's (1988) method, the lake is considered as a black target in the SPOT-XS3 band. The visibility value, and therefore aero-
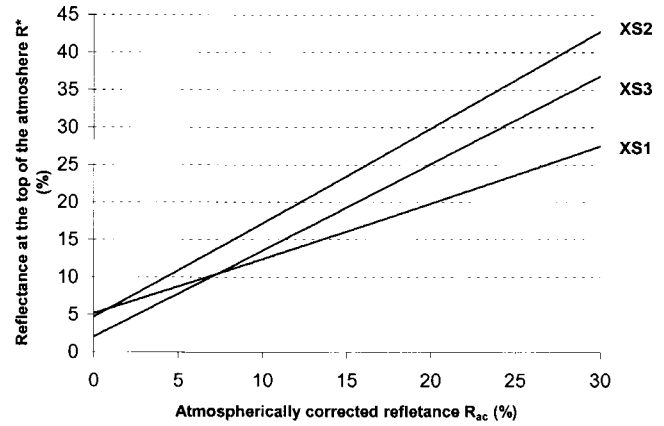

Fig. 4. Relationships between reflectance at the top of the atmosphere (R^*) and atmospherically corrected reflectance (R_{ac}) established with the 6s software (Vermote et al., 1997) and corresponding to corrections for the SPOT scene recorded 14/07/96, 11:23 UT.

sol optical thickness, is adjusted until the atmospherically corrected NIR reflectance was zero. The beaches have very high reflectances in the HRV-SPOT bands. Atmospherically corrected reflectances were compared to in situ reflectance values.

In Fig. 4, TOA reflectances are plotted versus atmospherically corrected reflectances, corresponding to corrections established for the SPOT image taken on 14/07/96. The relationships are almost linear in each SPOT spectral band, as the atmosphere is considered homogenous and as the correction of skylight reflection is uniform over the whole estuary (small-scale reflection effects, resulting from surface roughness, are consequently neglected).

4. Spectral reflectance model

4.1. Theory

Interpretation of remote-sensing reflectance measurements as a function of water composition necessitates to relate R_{rs} to inherent optical properties (IOPs) of the water body.

R_{rs} can be written as a function of the irradiance reflectance just beneath the surface (R), according to (Morel & Gentili, 1993):

$$R_{rs} = \frac{(1-\rho)(1-\bar{\rho})}{n^2(1-\bar{r}R)}\frac{R}{Q}, \tag{14}$$

where (Morel & Gentili, 1996): ρ, the internal Fresnel reflectance, is equal to 0.021 for $\theta = 0$; $\bar{\rho}$, the air–water Fresnel reflection at the interface, typically amounts between 4% and 5%; n, is the refractive index of water ($= 1.34$); $\bar{r}$, the water–air reflection, is of the order of 0.48; R, the reflectance or irradiance reflectance, is defined as the ratio $E_u(0-)/E_d(0-)$, with $E_u(0-)$ and $E_d(0-)$ the upwelling and downwelling irradiances at null depth

denoted $0-$; $Q = E_u(0-)/L_u(0-)$, in steradians, would be π if the L_u distribution was isotropic, but may vary between approximately 3.1 and 5.6.

The dimensionless reflectance (R) can be related to the IOPs of the water body according to (Gordon, Brown, & Jacobs, 1975) (Eq. (15)):

$$R = f \frac{b_b}{a + b_b} \qquad (15)$$

where f is a coefficient varying with illumination conditions and water types, a (m^{-1}) and b_b (m^{-1}) are the absorption and backscattering coefficients of the water body, respectively. The commonly adopted value for f is the mean value 0.33, which is valid for zenith Sun and large variety of naturals waters (Morel & Prieur, 1977).

The ratio $\frac{(1-\rho)(1-\bar{\rho})}{n^2(1-\bar{r}R)}$ accounts for all the reflection and refraction effects at the air–water interface. $\frac{(1-\rho)(1-\rho)}{n^2}$ is approximately equal to 0.54 when $\theta = 0$. For Case 1 waters where reflectance (R) is lower than 0.1, the term $(1 - \bar{r}R)$ is generally assumed to be unity. For Case 2 waters, R is generally higher than 0.1 and the term $(1 - \bar{r}R)$ must be considered. Therefore, an approximate formulation of Eq. (14) is (Eq. (16)):

$$R_{rs} \approx \frac{0.54}{(1 - 0.48*0.33\frac{b_b}{a+b_b})} \frac{0.33}{Q} \frac{b_b}{a + b_b}$$
$$= \frac{0.18}{(1 - 0.16\frac{b_b}{a+b_b})} \frac{1}{Q} \frac{b_b}{a + b_b}. \qquad (16)$$

It indicates that R_{rs} is a function of Q^{-1} (which accounts for the bidirectional effects; Morel & Gentili, 1996) and [$b_b/(a+b_b)$] (which accounts for the IOPs).

4.2. Reflectan

ce model

A spectral (400–900 nm) reflectance model, presented by Forget, Ouillon, Lahet, and Broche (1999) for sediment-dominated Case 2 waters influenced by river inputs, is adapted to the Gironde estuarine waters, in order to better interpret our in situ measurements, i.e., to estimate the influence of the IOPs on R_{rs} and to explain the observed R_{rs} variations with increasing SPM concentration. The purpose is to simulate approximately the IOPs influencing the reflectance, namely, the absorption and backscattering coefficients, which are expressed as the sum of contributions from optically active constituents. Only contributions of sediments and yellow substance are considered, assuming that contribution of phytoplankton to reflectance is very small. The absorption and backscattering coefficients are written (Eqs. (17) and (18)):

$$a(\lambda) = a_w(\lambda) + a_y(\lambda) + a_s(\lambda) \qquad (17)$$

$$b_b(\lambda) = b_{bw}(\lambda) + b_{bs}(\lambda) \qquad (18)$$

where subscripts w, y, and s, respectively, stand for water, yellow substance, and sediment. Absorption by sediments was neglected by Forget et al. (1999), but is considered in this study as SPM concentration in the Gironde estuary is extremely high.

Values of $a_w(\lambda)$ are taken from Smith and Baker (1981) for the range 400–800 nm and are deduced from Hale and Querry (1973) for the range 800–900 nm. $a_y(\lambda)$ is modelled by (Bricaud, Morel, & Prieur, 1981) (Eq. (19)):

$$a_y(\lambda) = a_y(\lambda_0)\exp[-s(\lambda - \lambda_0) \qquad (19)$$

where wavelengths are expressed in nanometers, $\lambda_0 = 440$ nm, $s = 0.014$ nm^{-1}.

Absorption by sediments is modelled by (Bricaud & Stramsky, 1990):

$$a_s(\lambda) = a_s(\lambda_0)\exp[-k(\lambda - \lambda_0)] \qquad (20)$$

where $\lambda_0 = 440$ nm, k varies in the range $0.005 - 0.009$ nm^{-1} and the 0.009 is arbitrarily taken. $a_s(\lambda_0)$ is expressed as a function of SPM concentration (Cipollini & Corsini, 1994): $a_s(\lambda_0) = 0.042*(SPM/S)$, where S is a constant value ($= 3.327$) (Schmitz-Pieffer, Viehoff, & Grassl, 1990).

$b_{bw}(\lambda)$ is equal to one-half the total scattering coefficient $b_w(\lambda)$ (Morel, 1980) for the range 400–800 nm and is neglected at greater wavelengths. Light scattering by suspended particles is modelled using the Mie theory (Van de Hulst, 1957), which allows to express $b_{bs}(\lambda)$ by (Forget et al., 1999):

$$b_{bs}(\lambda) = \frac{3SPM}{2\rho_{SPM}\ln(\frac{D_{min}}{D_{max}})} \int_{D_{min}}^{D_{max}} Q_{bb}(D, m_r, \lambda)D^{-2}dD \qquad (21)$$

where ρ_{SPM} is the sediment density, D the diameter of sediment particles, and Q_{bb} the backscattering efficiency factor of sediment particles of refractive index m_r. A Junge particle size distribution of slope-4 (Nanu & Robertson, 1993) is assumed for the wide range of diameters $0.01 - 120$ μm ($D_{min} - D_{max}$), which include fine and flocculated particles. The sediment density is assumed to be 2600 kg m^{-3}. The refractive index of sediment particles is taken in the range 1.10–1.15, with a mean value of 1.125.

5. Results

5.1. Spectral signature of highly turbid waters

In situ optical measurements provide spectral signatures of Gironde estuarine waters of various SPM concentrations. Fig. 5 displays some typical remote-sensing reflectance (R_{rs}) spectra measured in 1996 and 1997. The following conclusions can be drawn: between 400 and 1000 nm, R_{rs} increases with turbidity; the maximum R_{rs} value increases from 0.028 sr^{-1} (SPM concentration of 35 mg l^{-1}) to
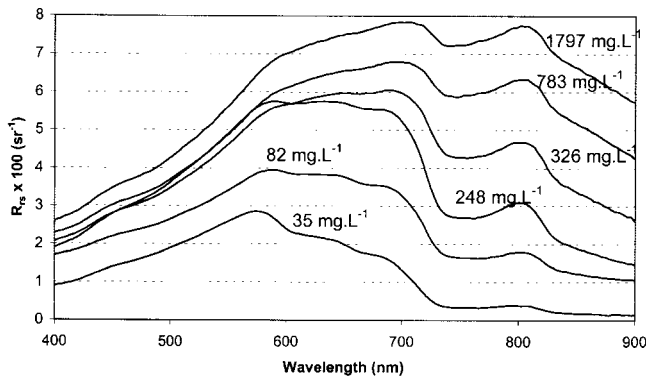
Fig. 5. Typical above-water reflectance spectra $R_{rs}(\lambda)$, corresponding to different SPM concentrations (mg l^{-1}). Spectra are normalized at 985 nm to correct for skylight reflection.

Fig. 7. Reflectance in XS1 band $R_{rs}(XS1) * 100$ versus SPM concentration. Between 0 and 500 mg l^{-1}, the function is logarithmic with a correlation factor of .741 ($a=0.455$, $b=0.514$).

0.078 sr^{-1} (1797 mg l^{-1}); the wavelength maximum increases from green to red and NIR wavelengths with increasing SPM concentration. From 35 to 250 mg l^{-1}, the reflectance increases between 400 and 700 nm and then, beyond 250 mg l^{-1}, the reflectance tends to saturate at these wavelengths, but strongly increases between 750 and 950 nm. A second R_{rs} maximum appears at 800 nm, that is characteristic of highly turbid waters as it was not yet observed in the Gironde plume, where SPM concentrations are lower (Froidefond et al., 1991). Reflectance is far from zero in the NIR (950–1000 nm) and clearly depends on SPM concentration.

According to Eq. (14), R_{rs} is a function of the IOPs, expressed by the ratio $[b_b/(a+b_b)]$. This ratio is modelled for a constant yellow substance concentration, expressed as $a_y(440\ nm)$. $a_y(440\ nm)$ is taken equal to 0.6 m^{-1}, which is representative of most of estuarine waters (Kirk, 1983). Variations of $[b_b/(a+b_b)]$ with wavelengths are computed for SPM concentrations of 35, 82, 248, 326, 783, and 1797 mg l^{-1} (Fig. 6). The maximum ratio value, obtained when SPM concentration is 1797 mg l^{-1}, is lower than 0.25 which involves the term $(1 - \bar{r}f[b_b/(a+b_b)])$ varies in the range of 0.96–1, with
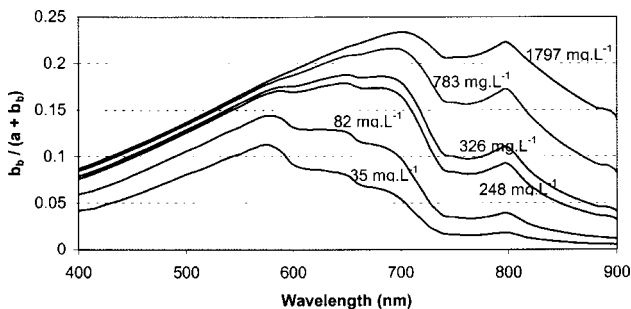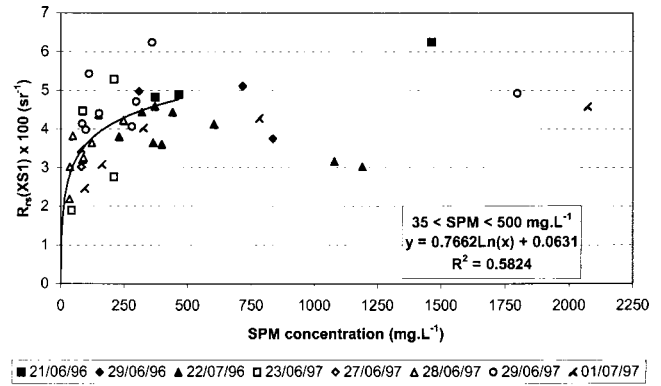
a mean value of 0.98 (with $\bar{r}=0.48$ and $f=0.33$). Eq (14) can be rewritten:

$$R_{rs} \approx \frac{0.178}{0.98}\frac{1}{Q}\frac{b_b}{a+b_b} = 0.182\frac{1}{Q}\frac{b_b}{a+b_b}. \qquad (22)$$

Comparison between the computed $[b_b/(a+b_b)]$ ratio (Fig. 6) and some of typical measured R_{rs} spectra (Fig. 5) shows that the adopted model parameters are approximate but realistic, and clearly demonstrates the predominant influence of the IOPs, which involves that variations due to bidirectional aspects are weak. As a consequence, most of variations observed on R_{rs} spectra can be explained with the considered reflectance model.

5.2. Empirical relationships

In 1996 and 1997, several R_{rs} measurements (42 in total) were taken in the estuary and related to SPM concentrations between 35 and 2072 mg l^{-1}. The $R_{rs}(\lambda)$ spectra were converted into SPOT equivalent remote-sensing reflectances $R_{rs}(XS1)$, $R_{rs}(XS2)$, and $R_{rs}(XS3)$. In total, the 42 points

Fig. 6. Computed $[b_b/(a+b_b)]$ ratio spectra for different pseudo-SPM concentrations. Values of model parameters: $m_r=1.125$; $(D_{min}, D_{max})=(0.1, 120)$ μm; a_y (440 nm)$=0.6$ m^{-1}.
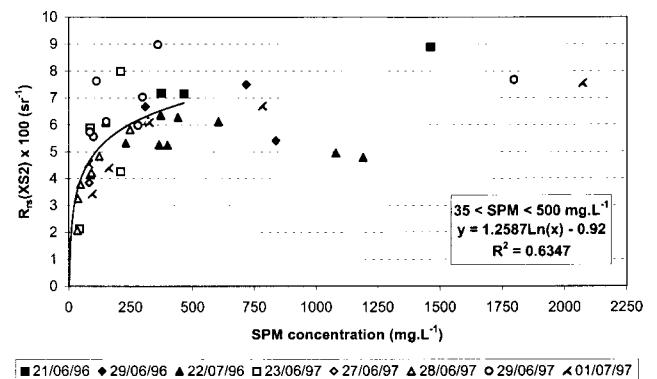

Fig. 8. Reflectance in XS2 band $R_{rs}(XS2) * 100$ versus SPM concentration. Between 0 and 500 mg l^{-1}, the function is logarithmic with a correlation factor of .857 ($a=-0.745$, $b=0.989$).
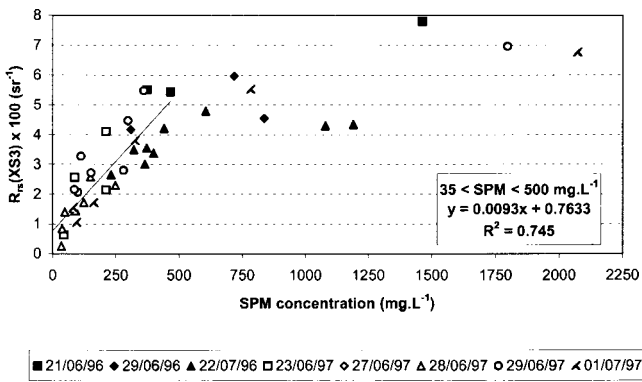
Fig. 9. Reflectance in XS3 band R_{rs}(XS3) * 100 versus SPM concentration. Between 0 and 500 mg l^{-1}, the function is linear with a correlation factor of .924 ($a = 0.136$, $b = 0.008$).

Fig. 11. Computed 0.33 $[b_b/(a + b_b)]$ ratio in XS2 band versus pseudo-SPM concentration, for three values of the sediment refractive index m_r. Values of other model parameters: $(D_{min}, D_{max}) = (0.1, 120)$ μm; a_y (440 nm) = 0.6 m^{-1}.

were used to develop empirical SPM algorithms in the concentration range 35–2072 mg l^{-1}. The relationships corresponding to XS1, XS2, and XS3 are presented in Figs. 7, 8, and 9, respectively, where the plotted curves are the best correlated functions between 35 and 500 mg l^{-1}. The legend on the graphs indicates the date of measurements.

For XS1 (Fig. 7), the reflectance first increases with increasing SPM concentration, quickly reaches a maximum level (0.062 sr^{-1} for 300 mg l^{-1}), then the signal becomes strongly variable (between 0.030 and 0.062 sr^{-1}) independently of SPM concentration and finally seems to decrease at extreme turbidity. A linear relationship is observed in the lowest concentrations (SPM < 50 mg l^{-1}), which is in agreement with results obtained by Froidefond et al. (1991). Between 35 and 500 mg l^{-1}, a logarithmic relationship with a correlation coefficient of .58 is found: R_{rs}(XS1) * 100 = 0.0631 + 0.7662 * ln(SPM). No acceptable correlation is found for the whole concentration range. For XS2 (Fig. 8), the reflectance is proportional to SPM at concentrations of up to 100 mg l^{-1}, reaches a maximum around 300 mg l^{-1}, then saturates and even decreases at extreme turbidities. Between 35 and 500 mg l^{-1}, a logarithmic relationship with a correlation coefficient of .63 is found: R_{rs}(XS2) * 100 = − 0.9200 +

1.2587 * ln(SPM). The reflectance variations, as a function of SPM concentration, are similar in the two visible spectral bands (XS1 and XS2): a logarithmic increase up to 500 mg l^{-1}, before saturation. The best correlation is found for XS3 (Fig. 9). The NIR reflectance is proportional to SPM concentration up to 500 mg l^{-1}, then decreases until 1300 mg l^{-1} and finally reaches a maximum value (around 0.07 sr^{-1}) for the highest concentrations (SPM >1500 mg l^{-1}). From 35 to 500 mg l^{-1}, the linear increase (plotted on the graph) is: R_{rs}(XS3) * 100 = 0.7633 + 0.0093 * SPM, with a correlation coefficient of .75. This relationship is in agreement with Moore et al. (1999) where the reflectance in MERIS band 14 (865 nm) was measured for fine sediment from the Humber estuary (UK) under laboratory conditions.

Skylight reflection does not significantly affect in situ measurements in SPOT spectral bands and the observed relationships are mainly due to the IOPs, expressed as the $[b_b/(a + b_b)]$ ratio. In order to explain R_{rs} variations in SPOT bands, the $[b_b/(a + b_b)]$ ratio is modelled in XS1, XS2, and XS3 for SPM concentration ranging from 25 to 2000 mg l^{-1}. Three refractive indexes of sediment particles (m_r) are considered (1.10, 1.125, and 1.15) to estimate the model sensitivity.
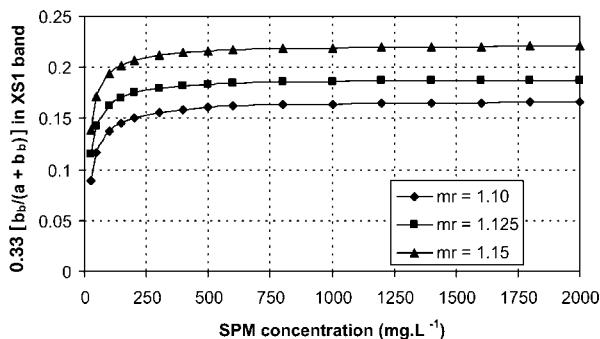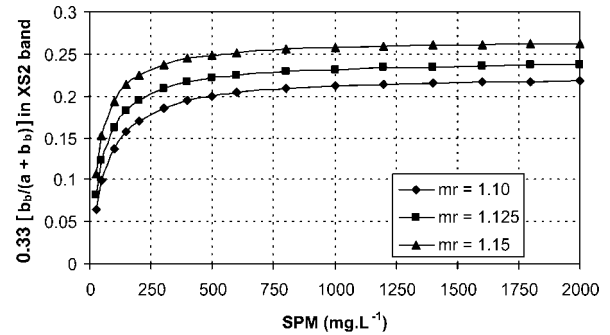

Fig. 10. Computed 0.33 $[b_b/(a + b_b)]$ ratio in XS1 band versus pseudo-SPM concentration, for three values of the sediment refractive index m_r. Values of other model parameters: $(D_{min}, D_{max}) = (0.1, 120)$ μm; a_y (440 nm) = 0.6 m^{-1}.
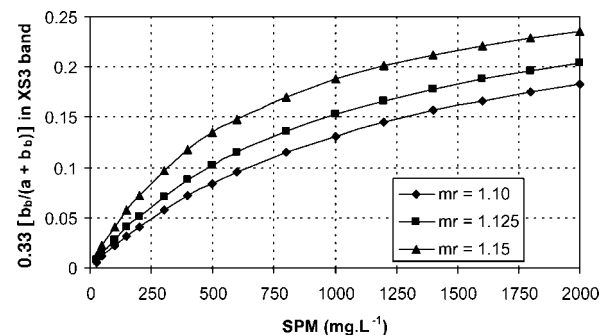

Fig. 12. Computed 0.33 $[b_b/(a + b_b)]$ ratio in XS3 band versus pseudo-SPM concentration, for three values of the sediment refractive index m_r. Values of other model parameters: $(D_{min}, D_{max}) = (0.1, 120)$ μm; a_y (440 nm) = 0.6 m^{-1}.

Table 2
Computed absorption (a,a_s) and backscattering (b_b,b_{bs}) coefficients in SPOT spectral bands for different pseudo-SPM concentrations

SPM (mg l^{-1})	XS1				XS2				XS3			
	a_s (m^{-1})	a (m^{-1})	b_{bs} (m^{-1})	b_b (m^{-1})	a_s (m^{-1})	a (m^{-1})	b_{bs} (m^{-1})	b_b (m^{-1})	a_s (m^{-1})	a (m^{-1})	b_{bs} (m^{-1})	b_b (m^{-1})
25	0.121	0.306	0.125	0.127	0.049	0.421	0.106	0.107	0.009	4.080	0.082	0.082
250	1.209	1.394	1.250	1.252	0.492	0.863	1.058	1.059	0.089	4.161	0.818	0.819
500	2.418	2.603	2.500	2.502	0.983	1.354	2.115	2.116	0.178	4.250	1.637	1.637
1500	7.254	7.439	7.500	7.502	2.949	3.321	6.346	6.347	0.533	4.606	4.911	4.911

Values of model parameters: $m_r = 1.125$; $(D_{min}, D_{max})=(0.1, 120)$ µm; a_y (440 nm) = 0.6 m^{-1}.

The modelled $[b_b/(a+b_b)]$ ratio increases from SPM concentration of 25 to 250 mg l^{-1} in XS1 band (Fig. 10), from 25 to 500 mg l^{-1} in XS2 (Fig. 11), then saturates for higher SPM concentrations, independently of m_r. In the XS3 band, $[b_b/(a+b_b)]$ increases with SPM concentration from 25 to 2000 mg l^{-1} (Fig. 12). Analysis of computed a, b_b, a_s, and b_{bs} coefficients (Table 2) shows that contribution of pure water to light backscattering can be neglected for the considered SPM concentration (>25 mg l^{-1}), which involves: $b_b \approx b_{bs}$. A second observation is that contribution of pure water and yellow substance to light absorption becomes insignificant in XS1 and XS2, when SPM concentration is higher than 250 and 500 mg l^{-1}, respectively, which involves $a \approx a_s$. In XS3, absorption by pure water is always predominant compared to absorption by sediments. When contribution of pure water and yellow substance to light absorption is significant, the $[b_b/(a+b_b)]$ ratio can be written:

$$\frac{b_b}{a+b_b} = \frac{b_{bs}}{(a_w+a_y)+a_s+b_{bs}} \qquad (23)$$

According to Eqs. (20) and (21), $a_s(\lambda)$ and $b_{bs}(\lambda)$ are both proportional to SPM concentration, and can be written: $a_s(\lambda) = SPMf_1(\lambda)$; $b_{bs}(\lambda) = SPMf_2(\rho_{SPM}, D, m_r, \lambda)$, where f_1 and f_2 are functions independent of SPM concentration. Eq. (23) becomes (Eq. (24)):

$$\frac{b_b}{a+b_b} = \frac{SPMf_2}{(a_w+a_y)+SPM(f_1+f_2)}. \qquad (24)$$

It explains why the $[b_b/(a+b_b)]$ ratio, and therefore the R_{rs} measurements, increases with increasing SPM concentration in XS1 (25 < SPM < 250 mg l^{-1}), in XS2 (25 < SPM < 500 mg l^{-1}) and in XS3 (25 < SPM < 2000 mg l^{-1}).

When contribution of pure water and yellow substance to light absorption becomes insignificant, the $[b_b/(a+b_b)]$ ratio can be written (Eq. (25)):

$$\frac{b_b}{a+b_b} = \frac{b_{bs}}{a_s+b_{bs}} = \frac{SPMf_2}{SPM(f_1+f_2)} = \frac{f_2}{f_1+f_2} \qquad (25)$$

The $[b_b/(a+b_b)]$ ratio, and therefore the R_{rs} measurements, becomes independent of SPM concentration, which

explains the saturations observed in XS1 (SPM >250 mg l^{-1}) and in XS2 (SPM >500 mg l^{-1}).

The computed $[b_b/(a+b_b)]$ ratio in XS1, XS2, and XS3 is highly sensitive to variations of m_r. The range of particle grain-size $(D_{min} - D_{max})$, which was supposed invariant in our computations, is another sensitive model parameter (Forget et al., 1999). The variations of m_r and $(D_{min} - D_{max})$, which probably occurred during our in situ measurements, can explain irregularities observed in Figs. 7–9.

Changes in sediment composition and grain-size, which directly influence $[b_b/(a+b_b)]$ and R_{rs} in a single band through the b_{bs} coefficient, can be reduced when considering reflectance ratios (Moore et al., 1999). In fact, assuming that $b_b \approx b_{bs}$ for SPM concentration greater than 25 mg l^{-1} and that spectral variations of b_{bs} are weak, the ratio $\Re(XS3i)=[(b_b/(a+b_b))(XS3)/(b_b/(a+b_b))(XSi)]$ (where $i=1$ for XS1 and $i=2$ for XS2) is written (Eq. (26)):

$$\Re(XS3i) \approx \frac{b_{bs}(XS3)}{b_{bs}(XSi)} \frac{a(XSi)+b_{bs}(XSi)}{a(XS3)+b_{bs}(XS3)}$$

$$\approx \frac{a(XSi)+b_{bs}(XSi)}{a(XS3)+b_{bs}(XS3)} \qquad (26)$$

The contribution of the b_{bs} coefficient to $\Re(XS3i)$ ratios is limited. As a result, when the computed $\Re(XS31)$ and $\Re(XS32)$ ratios are plotted versus SPM concentration (Figs. 13 and 14), it appears that influence of m_r variations

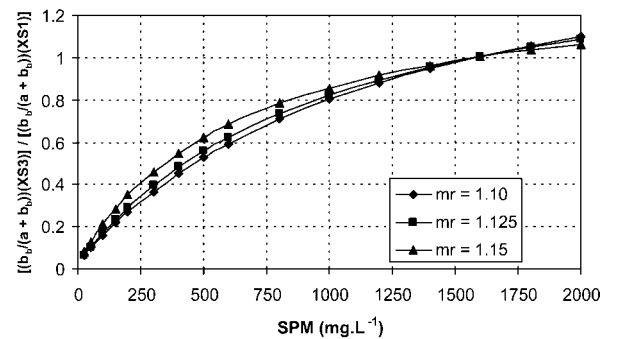Fig. 13. Computed $[(b_b/(a+b_b))(XS3)/(b_b/(a+b_b))(XS1)]$ ratio versus pseudo-SPM concentration, for three values of the sediment refractive index m_r. Values of other model parameters: $(D_{min}, D_{max})=(0.1, 120)$ µm; a_y (440 nm) = 0.6 m^{-1}.
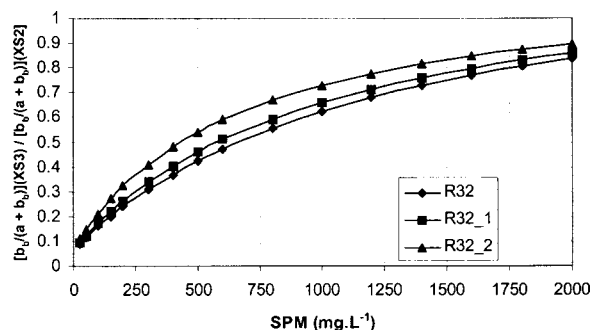
Fig. 14. Computed $[(b_b/(a+b_b))(XS3)/(b_b/(a+b_b))(XS2)]$ ratio versus pseudo-SPM concentration, for three values of the sediment refractive index m_r. Values of other model parameters: $(D_{min}, D_{max})=(0.1, 120)\,\mu m$; a_y (440 nm) = 0.6 m^{-1}.

are notably reduced. According to Eq. (22), remote-sensing reflectance ratios are written (Eq. (27)):

$$\frac{R_{rs}(XS3)}{R_{rs}(XSi)} = \frac{Q(XS3)}{Q(XSi)}\Re(XS3i)$$ (27)

Consequently, these R_{rs} ratios will be seldom affected by variations of m_r. This assumption is confirmed by in situ R_{rs} measurements: the $[R_{rs}(XS3)/R_{rs}(XS1)]$ (Fig. 15) and $[R_{rs}(XS3)/R_{rs}(XS2)]$ (Fig. 16) ratios are well correlated to SPM concentration. Moreover, the obtained relationships include all in situ measurements completed during the different field campaigns within the ±0.011 sr^{-1} (Fig. 15) and ±0.007 sr^{-1} (Fig. 16) function uncertainties. The influence of particle grain-size and refractive index variations, which directly affect reflectance in SPOT bands, is therefore reduced when considering reflectance ratios. Comparison between the measured R_{rs} ratios (Figs. 15 and 16) and the modelled $\Re$ ratios (Figs. 13 and 14), plotted versus SPM concentration, confirms once again that variations of the Q

21/06/96 ◆ 29/06/96 ▲ 22/07/96 ☐ 23/06/97 ◇ 27/06/97 △ 28/06/97 ○ 29/06/97 ✗ 01/07/97
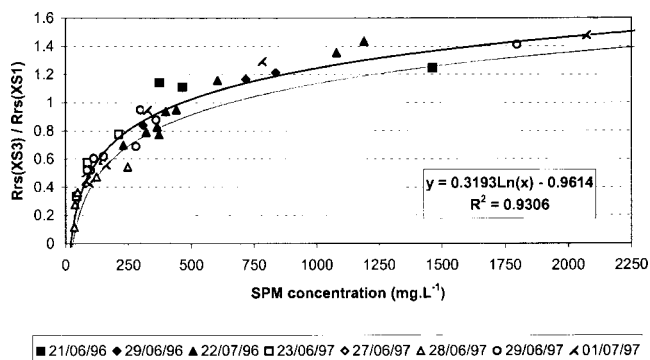
Fig. 15. $R_{rs}(XS3)/R_{rs}(XS1)$ band ratio versus SPM concentration. The function is logarithmic (second rate) with a correlation factor of .935 ($a = -0.5014$, $b = 0.03983$).

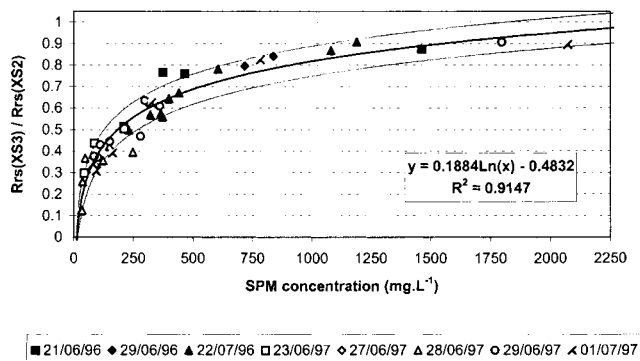21/06/96 ◆ 29/06/96 ▲ 22/07/96 ☐ 23/06/97 ◇ 27/06/97 △ 28/06/97 ○ 29/06/97 ✗ 01/07/97

Fig. 16. $R_{rs}(XS3)/R_{rs}(XS2)$ band ratio versus SPM concentration. The function is logarithmic with a correlation factor of .917 ($a = -0.7063$, $b = 0.2168$).

function are weak. The established relationship (Fig. 15) is written:

$$\frac{R_{rs}(XS3)}{R_{rs}(XS1)} = 0.3193\ln(SPM) - 0.9614$$ (28)

with a correlation factor of .9306. The function is logarithmic between 35 and 2250 mg l^{-1} and shows a linear increase in this ratio at SPM concentrations lower than 500 mg l^{-1}, then a more moderate increase for higher concentrations (from 500 to 2250 mg l^{-1}).

The second relationship (Fig. 16):

$$\frac{R_{rs}(XS3)}{R_{rs}(XS2)} = 0.1884\ln(SPM) - 0.4832$$ (29)

has a correlation factor of .9147. The function is also logarithmic; a linear increase is observed for the lower

Table 3
SPM concentrations determined from the $[R_{rs}(XS3)/R_{rs}(XS1)]$ reflectance ratio

$R_{rs}(XS3)/$ $R_{rs}(XS1)$	Mean SPM concentration (mg l^{-1})	Minimum SPM concentration (mg l^{-1})	Maximum SPM concentration (mg l^{-1})	Uncertainty (%)
0.2	38	28	53	32.9
0.3	52	37	73	34.6
0.4	71	51	100	34.5
0.5	97	69	137	35.0
0.6	133	95	187	34.6
0.7	182	130	255	34.3
0.8	249	176	350	34.9
0.9	340	241	480	35.1
1.0	465	330	656	34.9
1.1	635	451	900	35.3
1.2	870	617	1228	35.1
1.3	1187	842	1680	35.3
1.4	1627	1155	2297	35.1
1.5	2225	1578	3135	35.0

The given mean, minimum, and maximum SPM (mg l^{-1}), and the percentage error (%) are deduced from the uncertainties presented in Fig. 8.

concentrations (SPM <500 mg 1^{-1}), then the increase is logarithmic and finally, the reflectance ratio reaches its maximum value of 0.9.

These empirical relationships are obtained with high correlation coefficients ($>.9$) and the ± 0.011 and ± 0.007 sr^{-1} and include most points, independently of the date of measurement. They are consequently robust to determine SPM concentrations from above-water reflectance measurements, at least for the period covered by the field campaigns (1996 and 1997 summers). The percentage errors associated with the retrieved SPM concentrations from Eq. (28) (Table 3) and Eq. (29) (Table 4) are lower than 38%.

5.3. SPM concentrations

From all in situ measurements completed in 1996 and 1997 summers, a single relationship was obtained between SPM concentration and the reflectance band ratio [R_{rs}(XS3)/R_{rs}(XS2)]). This relationship is consequently valid at least for the 1996 and 1997 summer periods and can be applied to a SPOT scene taken during this time, even if no in situ measurements were performed during the satellite overpass.

The algorithm is applied to the SPOT image taken on the 14th of July 1996. Satellite data recorded in XS2 and XS3 bands are corrected for atmospheric effects. Reflectance band ratio [R_{ac}(XS3)/R_{ac}(XS2)] values are converted to SPM concentrations according to Eq. (29) (Fig. 16). SPM concentrations are quantified with uncertainties indicated (Table 4). Only the downstream part of the estuary is presented (Fig. 17) and the geographical borders of the area are defined in Fig. 1.

The imagery was acquired during a period of low river flow and according to the sedimentology knowledge of the estuary (Castaing, 1981; Sottolichio et al., 2001), the turbidity maximum would have been located between Pauillac and Bordeaux (Fig. 1).

At image acquisition time, the upstream and central parts of the estuary (PK 20–PK 70) were influenced by ebb tide

Fig. 17. SPOT-XS image (@CNES 14/07/96, 11:23 TU) of the downstream part of the Gironde estuary. The presented area is located in Fig. 1. The SPM concentrations were calculated from relationship presented in Fig. 10.

currents and the downstream part (PK 70–PK 90) had a slack tide, with the flood tide starting in the mouth.

SPM concentrations, detected from satellite data (Fig. 17), decrease from upstream to downstream (from the right to the left on the image), ranging from more than 700 mg 1^{-1} to approximately 20 mg 1^{-1}. The highest SPM concentrations are found along the navigation channel (C) and right-hand shore banks (D) where ebb tide currents reach their maximum velocity, erode recently settled sediment, and transport it downstream. The lowest concentrations (SPM <100 mg 1^{-1}) are located in the downstream part of the estuary: the slow (slack tide) currents cannot transport suspended particles, which fall and settle. The flood tide, starting near the mouth, brings clear oceanic water into the estuary. The Talais and Marguerites banks (A and B) have high SPM concentrations (around 300 mg 1^{-1}), which probably result from resuspension over shallow waters. Downstream, along the estuary shore, underwater mud banks appear as clear areas (F).

These observations are in good agreement with previous knowledge of the estuarine sedimentology (Castaing, 1981; Sottolichio et al., 2001) and tidal data. The navigation channel is easily located and starts with a stretched turbulent flow created by the strong ebb current (C). Progressively, the flow widens with decreasing current velocity (E), and follows the channel morphology. Upstream, sedimentary flows are longitudinal and parallel to the shore, as a result of strong ebb currents that transport SPM from the turbidity maximum towards the centre and downstream parts of the estuary.

Table 4
SPM concentrations determined from the [R_{rs}(XS3)/R_{rs}(XS2)] reflectance ratio

R_{rs}(XS3)/ R_{rs}(XS2)	Mean SPM concentration (mg l^{-1})	Minimum SPM concentration (mg l^{-1})	Maximum SPM concentration (mg l^{-1})	Uncertainty (%)
0.2	38	26	54	36.8
0.3	64	44	93	38.3
0.4	109	75	156	37.2
0.5	185	128	266	37.3
0.6	313	216	455	38.2
0.7	535	370	770	37.4
0.8	905	625	1310	37.8
0.9	1540	1065	2235	38.0
1.0	2620	1815	3805	38.0

The given mean, minimum, and maximum SPM (mg l^{-1}), and the percentage error (%) are deduced from the uncertainties presented in Fig. 9.

Downstream, flows are wider, moving slowly towards the right-hand shore. Oceanic clear water intrusions at the mouth are opposed to the declining sedimentary flows. The features observed within the shallow waters, over mud banks and sandbanks (A and B) and along the shorebanks (D) probably result from resuspension.

6. Discussion and conclusions

An experimental methodology was used to interpret "ocean colour" satellite data of highly turbid waters, the Gironde estuary, and a relationship between remote-sensing reflectance and SPM concentration was established. The satellite data were corrected for atmospheric effects, using radiative transfer code and in situ reflectance measurements, and then converted to SPM concentrations.

The main advantage of the method is the direct comparison of in situ radiometric measurements (radiance or equivalent remote-sensing reflectance) and the concentrations of optically active substances, but it requires an accurate knowledge of the water body and sufficient in situ measurements. The in situ measurements describe the spectral variation of remote-sensing reflectance $R_{rs}(\lambda)$ with SPM: $R_{rs}(\lambda)$ increases with SPM concentration, first at the lower wavelengths (400–600 nm), then in the middle wavelengths (600–700 nm), and finally, in the NIR domain (700–900 nm); a characteristic maximum reflectance appears at 800 nm.

The methodology was applied to the Gironde estuary, using HRV-SPOT data. The SPOT visible band (XS1 and XS2) reflectances were poorly correlated with SPM, but showed a logarithmic increase up to 500 mg l^{-1} and then saturation. This result indicated that the skylight reflection effects were significant, but the IOPs mainly influenced the relationships. The R_{rs}(XS3) band, the R_{rs}(XS3)/R_{rs}(XS1) ratio, and the R_{rs}(XS3)/R_{rs}(XS2) ratio were highly correlated with SPM concentration. The use of remotely sensed reflectance ratios reduced skylight reflection and was therefore used instead of a single band. As a result, SPM was quantified to a high precision ($\pm 35\%$).

The SPOT-HRV data showed detailed sedimentary flows in the estuary, with the suspended particles acting as excellent currents markers, as the mean settling velocity was low (about 1 mm/s). The particle's capability to backscatter incident light in visible and NIR wavelengths produced strong reflectance signals, and therefore, high SPM concentrations appeared as bright areas in the image.

In conclusion, sedimentary flows are predominant features in the estuary and move within the surface waters; SPOT data can be used to rapidly locate the turbidity maximum, erosion and deposition areas; suspended particles can act as currents markers, providing observations of hydrodynamic features.

Future developments include improvements to the atmospheric correction: the inclusion of small-scale reflection effects (induced by the surface roughness) and Rayleigh/aerosol interaction. The methodology will also be applied to Landsat-7 data, which have seven spectral bands in the visible and infrared wavelengths, and a high spatial resolution suitable to estuaries. Supplementary homogeneous targets near the Gironde estuary will be used to improve and validate the atmospheric corrections.

Acknowledgments

References

Abril, G., Etcheber, H., Le Hir, P., Bassoullet, P., Boutier, B., & Frankignoulle, M. (1999). Oxic/anoxic oscillations and organic carbon mineralization in an estuarine maximum turbidity zone (The Gironde, France). Limnology and Oceanography, 44 (5), 1304–1315.

Allen, G. P., Salomon, J. C., Bassoullet, P., Du Penhoat, Y., & Degranpré, C. (1980). Effects of tides on mixing and suspended sediment transport in macrotidal estuaries. Sedimentary Geology, 26, 69–90.

Allen, G. P., Sauzay, G., Castaing, P., & Jouanneau, J. M. (1977). Sediment transport processes in the Gironde estuary. In: M. Wilet (Ed.), Estuarine processes (pp. 63–81). New York: Academic Press.

Anji Reddy, M. (1993). Remote sensing for mapping of suspended sediments in Krishna Bay Estuary, Andhra Pradesh, India. International Journal of Remote Sensing, 14 (11), 2215–2221.

Antoine, D., Morel, A., & André, J. M. (1995). Algal pigment distribution and primary production in the eastern Mediterranean as derived from coastal zone color scanner observations. Journal of Geophysical Research, 100 (C8), 16193–16209.

Austin, R. W. (1974). Inherent spectral radiance signatures of the ocean surface. In: Ocean color analysis (195 pp.). La Jolla, CA: Scripps Institute of Oceanography (Refs. 74-10).

Bricaud, A., Morel, A., & Prieur, L. (1981). Absorption by dissolved organic matter of the sea (yellow substance) in the UV and visible domains. Limnology and Oceanography, 26 (1), 43–53.

Bricaud, A., & Stramski, D. (1990). Spectral absorption coefficients of living phytoplankton and nonalgal biogenous matter: a comparison between the Peru upwelling area and the Sargasso Sea. Limnology and Oceanography, 35 (3), 562–582.

Castaing, P. (1981). Le transfert à l'océan des suspensions estuariennes. Cas de la Gironde. PhD thesis, University Bordeaux I, no. 701, 605 pp.

Castaing, P., & Allen, G. P. (1981). Mechanisms of seaward escape of suspended sediment from the Gironde: a macro tidal estuary in France. Marine Geology, 40, 101–118.

Chavez Jr., P. S. (1988). An improved dark-object substraction technique for atmospheric scattering correction of multispectral data. Remote Sensing of Environment, 24, 459–479.

Cippollini, P., & Corsini, G. (1994). The effect of yellow substance on pigment concentration retrieval using "blue and green" ratio. IEEE International Geoscience and Remote Sensing, 772–777.

Dilligeard, E. (1997). Télédétection des eaux du cas II; caractérisations des sédiments marins. PhD thesis, University of Littoral, Côte d'Opale, 184 pp.

Eisma, D., Bernard, P., Cadée, G. C., Ittekkot, V., Kalf, J., Lanne, R., Martin, J. M., Mook, W. G., Put, A., & Schuhmacher, T. (1991). Suspended

matter particle size in some West-European estuaries: Part II. A review on floc formation and break up. *Netherlands Journal of Sea Research, 28* (3), 215–220.

Eisma, D., & Li, A. (1993). Changes in suspended matter floc size during the tidal cycle in the Dollard Estuary. *Netherlands Journal of Sea Research, 31* (2), 107–117.

Forget, P., & Ouillon, S. (1998). Surface suspended matter off the Rhône river mouth from visible satellite imagery. *Oceanologica Acta, 21* (6), 739–749.

Forget, P., Ouillon, S., Lahet, F., & Broche, P. (1999). Inversion of reflectance spectra of non-chlorophyllous turbid coastal waters. *Remote Sensing of Environment, 68*, 264–272.

Fougnie, B., Frouin, R., Lecomte, P., & Deschamps, P. Y. (1999). Reduction of skylight reflection effects in the above-water measurements of diffuse marine reflectance. *Applied Optics, 38*, 3844–3856.

Froidefond, J. M., Castaing, P., Mirmand, M., & Ruch, P. (1991). Analysis of the turbid plume of the Gironde (France) based on SPOT radiometric data. *Remote Sensing of Environment, 36*, 149–163.

Gordon, H. R., Brown, O. B., & Jacobs, M. M. (1975). Computed relations between the inherent and apparent optical properties of a flat homogeneous ocean. *Applied Optics, 14*, 417–427.

Gordon, H. R., & McCluney, W. R. (1975). Estimation of the sunlight penetration in the sea for remote sensing. *Applied Optics, 14*, 413–416.

Hale, G. M., & Querry, M. R. (1973). Optical constants of water in the 200 nm to 200 μm wavelength region. *Applied Optics, 12*, 555–563.

Irigoien, X., & Castel, J. (1997). Light limitation and distribution of chlorophyll pigments in a highly turbid estuary: the Gironde (SW France). *Estuarine, Coastal and Shelf Science, 44*, 507–517.

Ivanoff, A. (1975). *Introduction à l'océanographie, tome II*, Edition Vuibert, 340 pp.

Jouanneau, J. M., & Latouche, Cl. (1981). The Gironde Estuary. *Contributions to Sedimentology, vol. 10* (115 pp.). Springer-Verlag.

Kirk, J. T. O. (1983). *Light and photosynthesis in aquatic ecosystems*. Cambridge: Cambridge University Press (509 pp.).

McClatchey, R. A., Fenn, R. W., Selby, J. E. A., Volz, F. E., Garing, J. S. (1971). *Optical properties of the atmosphere (revised)*. AFCRL 71-0279, Env. Research Paper 354, Bedforf, MA, USA.

Mobley, C. D. (1999). Estimation of the remote-sensing reflectance from above-surface measurements. *Applied Optics, 38*, 7442–7455.

Moore, G. F., Aiken, J., & Lavender, S. J. (1999). The atmospheric correction of water colour and the quantitative retrieval of suspended particulate matter in Case II waters: application to MERIS. *International Journal of Remote Sensing, 20*, 1713–1733.

Morel, A. (1980). In-water and remote sensing measurements of ocean color. *Boundary-Layer Meteorology, 18*, 177–201.

Morel, A. (1988). Optical modelling of the upper ocean in relation to its biogenous matter content (Case I waters). *Journal of Geophysical Research, 93* (C9), 10749–10768.

Morel, A. (1991). Optics of marine particles and marine optics. *Optical Aspects of Oceanography, NATO ASI Series, G27*, 141–188.

Morel, A., & Gentili, B. (1993). Diffuse reflectance of oceanic waters: II. Bidirectional aspects. *Applied Optics, 32*, 6864–6879.

Morel, A., & Gentili, B. (1996). Diffuse reflectance of oceanic waters: II. Implication of bidirectionality for the remote-sensing problem. *Applied Optics, 35*, 4850–4861.

Morel, A., & Prieur, L. (1977). Analysis of variations in ocean color. *Limnology and Oceanography, 22*, 709–722.

Nanu, L., & Robertson, C. (1993). The effect of suspended sediment depth distribution on coastal water spectra reflectance: theoretical simulation. *International Journal of Remote Sensing, 14* (2), 225–239.

O'Reilley, J. E., Maritorena, S., Mitchell, B. G., Siegel, D. A., Carder, K. L., Garver, S. A., Kahru, M., & McClain, C. (1998). Ocean color chlorophyll algorithm for SeaWiFS.. *Journal of Geophysical Research, 103* (C11), 24937–24953.

Ouillon, S., Forget, P., Froidefond, J. M., & Naudin, J. J. (1997). Estimating suspended matter concentrations from SPOT data and from field measurements in the Rhône river plume. *Marine Technology Society Journal, 31* (2), 15–20.

Robinson, M. C., Morris, K. P., & Dyer, K. R. (1998). Deriving fluxes of suspended particulate matter in the Humber estuary, UK, using airborne remote sensing. *Marine Pollution Bulletin, 37* (3–7), 155–163.

Schmitz-Pieffer, A., Viehoff, T., & Grassl, H. (1990). Remote sensing of coastal waters by airborne lidar and satellite radiometer: Part 2. Measurements. *International Journal of Remote Sensing, 11*, 2185–2204.

Siegel, H., Gerth, M., & Mutzke, A. (1999). Dynamics of the Oder river plume in the Southern Baltic Sea: satellite data and numerical modelling. *Continental Shelf Research, 19*, 1143–1159.

Smith, R. C., & Baker, A. (1981). Optical properties of the clearest natural waters (200–800 nm). *Applied Optics, 20*, 177–184.

Sottolichio, A., Le Hir, P., & Castaing, P. (2001). Modelling mechanisms for the turbidity maximum stability in the Gironde estuary, France. Coastal and estuarine fine sediment transport processes. In: W. H. McAnally, & A. J. Mehta (Eds.), (pp. 373–385). Amsterdam: Elsevier.

Van de Hulst, H. C. (1957). *Light scattering by small particles*. New York: Dover (470 pp.).

Vermote, E. F., Tanre, D., Deuze, J. L., Herman, M., & Morcrette, J. J. (1997). Second simulation of the satellite signal in the solar spectrum: an overview. *IEEE Transactions on Geoscience and Remote Sensing, 35* (3), 675–686.

Weber, O., Jouanneau, J. M., Ruch, P., & Mirmand, M. (1991). Grain-size relationship between suspended matter originating in the Gironde estuary and shelf mud-patch deposits. *Marine Geology, 96*, 159–165.

Whitlock, C. H., Poole, L. R., Usry, J. W., Houghton, W. M., Witte, W. G., Morris, W. D., & Gurganus, E. A. (1981). Comparison of reflectance with backscatter and absorption parameters for turbid waters. *Applied Optics, 20*, 517–522.